Microlensing mass measurement from images of rotating gravitational arcs †

Arnaud Cassan[1,⋆], Clément Ranc[1,2], Olivier Absil[3], Łukasz Wyrzykowski[4], Krzysztof A. Rybicki[4], Étienne Bachelet[5], Jean-Baptiste Le Bouquin[6,7], Markus Hundertmark[8], Rachel Street[5], Jean Surdej[3,9], Yiannis Tsapras[8], Joachim Wambsganss[8] and Olivier Wertz[3]

(1) Institut d'Astrophysique de Paris, Sorbonne Université, CNRS, UMR 7095, 98 bis bd Arago, F-75014 Paris, France

(2) Astrophysics Science Division, NASA/Goddard Space Flight Center, Greenbelt, MD 20771, USA

(3) Space sciences, Technologies and Astrophysics Research (STAR) Institute, University of Liège, Belgium

(4) Astronomical Observatory, University of Warsaw, Al. Ujazdowskie 4, 00-478 Warszawa, Poland

(5) Las Cumbres Observatory Global Telescope Network, 6740 Cortona Drive, suite 102, Goleta, CA 93117, USA

(6) Université Grenoble Alpes, CNRS, IPAG, F-38000 Grenoble, France

(7) Department of Astronomy, University of Michigan, 1085 S. University, Ann Arbor, MI 48109, USA

(8) Zentrum für Astronomie der Universität Heidelberg, Astronomisches Rechen-Institut, Mönchhofstr. 12-14, 69120 Heidelberg, Germany

(9) Astronomical Observatory Institute, Faculty of Physics, Adam Mickiewicz University, ul. Sloneczna 36, 60-286 Poznań, Poland

(⋆) Corresponding author. Email: cassan@iap.fr

†This version of the article has been accepted for publication, after peer review but is not the Version of Record and does not reflect post-acceptance improvements, or any corrections. The Version of Record is available online at: `http://dx.doi.org/10.1038/s41550-021-01514-w`. Use of this Accepted Version is subject to the publisher's Accepted Manuscript terms of use `https://www.springernature.com/gp/open-research/policies/accepted-manuscript-terms`.

Gravitational microlensing [1] is a powerful technique for measuring the mass of isolated and faint or non-luminous objects in the Milky Way [2, 3]. In most cases, however, additional observations to the photometric light curve are required to measure accurately the mass of the microlens. Long-baseline optical/infrared interferometry provides a new and efficient way to deliver such independent constraints [4, 5, 6, 7], as demonstrated recently by first interferometric observations in microlensing event TCP J05074264+2447555 ('Kojima-1') [8]. Here, we report real-time observations of gravitationally lensed arcs in rotation around a microlens, Gaia19bld [9], made with the PIONIER instrument [10] at the Very Large Telescope Interferometer. Our data allowed us to determine the angular separation and length of the arcs, as well as their rotation rate. Combining these measurements with ground-based photometric data enabled the determination of the microlens mass, $M = 1.147 \pm 0.029\,\mathrm{M}_\odot$, to a very high accuracy. We anticipate interferometric microlensing to play an important future role in the mass and distance determination of isolated stellar-mass black holes [11, 12, 13] in the Galaxy, which cannot be addressed by any other technique.

In Galactic microlensing, a foreground massive object (the 'microlens') crosses the line-of-sight of a background 'source' star, and splits its disk-shaped image into multiple and distorted images. What is actually observed by photometric monitoring is an increase of the total light received from the source (called 'magnification') as its alignment with the microlens and the observer improves, followed by a decrease when they move apart due to their relative motion. In a notebook from 1912, Einstein described this phenomenon as the 'lens-like action' of the foreground star, but his calculations were not published until 1936 for he was convinced that there was 'no hope of observing this phenomenon directly' [14]. The first microlensing events were yet reported in 1993, and today several thousands of events have been observed, the larger fraction of which in the last decade. In practice, single microlenses produce a characteristic bell-shape light curve, while microlenses made of multiple bodies lead to more complex ones. As microlensing does not rely on the light emitted by the microlenses themselves, potential detections include distant bound and free-floating exoplanets, faint brown dwarfs and white dwarfs as well as neutron stars and stellar-mass black holes [15].

Measuring the microlens mass requires two quantities to be measured: π_E, the microlens parallax, and θ_E, the angular Einstein ring radius (that is, the radius of the ring-like image of the source, would it be perfectly aligned with the microlens). The mass follows from [2] $M = \theta_\mathrm{E}/(\kappa\pi_\mathrm{E})$, with $\kappa = 8.144$ mas/$\mathrm{M}_\odot$ (1 mas = 1 milli-arcsecond) and $\mathrm{M}_\odot$ the mass of the Sun. Ground-based observa-

tions can access $\pi_{\rm E}$ for long-lasting microlensing events, for which the transverse motion of the Earth is significant enough to allow a good parallax measurement. For shorter microlensing events, and for accurate parallax measurements in general, space parallax is required and indeed, several such observations were made in the recent years by the Spitzer Space Telescope [16]. The second quantity, $\theta_{\rm E}$, is usually measured when the light curves exhibits finite source effects, *i.e.* when the radius of the source in $\theta_{\rm E}$ units, ρ, can be estimated from the light curve modelling. This requires, however, the source to transit a region of gravitational caustics (producing local magnification peaks in the light curve), which for isolated microlenses only concerns high-magnification events. In the case of bright microlenses, high-resolution, adaptive-optics imaging can also access $\theta_{\rm E}$ typically 5-10 years after the microlensing event is over, when the background star and the microlens can be resolved individually [17]. To date, this has been achieved for a dozen microlensing events.

An alternative route to measure the angular Einstein ring radius is to resolve directly the split images of the source star, as their angular separation is closely related to $\theta_{\rm E}$ (Methods). While the typical separation of the microlensed images ($\sim$ 1 mas) remains well below the resolution of classical telescopes, it is within the reach of long-baseline infrared interferometers [4, 5, 6, 7] equipped with the latest generation of instruments [10]. An important advantage of interferometry over previous techniques is that it does not request the microlens to be luminous or to transit caustics. Microlensing event 'Kojima-1' was the first to be observed by interferometry with GRAVITY at the VLTI [8], for which the authors reported the resolution of the two point-like images of the source star from a single epoch of interferometric closure phases. However, as the separation and alignement of the two images depends on time, in that case the derived value of $\theta_{\rm E}$ partly relied on the details of the light curve modelling. Two possible values were actually found [8], depending on the chosen model $\theta_{\rm E} = 1.850 \pm 0.014$ mas and $\theta_{\rm E} = 1.891 \pm 0.014$ mas (or $\theta_{\rm E} = 1.87 \pm 0.03$ mas considering both models). Further follow-up studies [18, 19] using complementary ground-based data, Gaia and Spitzer space data, as well as Keck adaptive-optics images and spectroscopic data were used to break the degeneracy in the models, yielding a determination of the microlens mass to a relative uncertainty of about 6%.

Here we report the first times-series interferometric observations of a microlensing event, Gaia19bld, using PIONIER at the VLTI. Both closure phases and squared visibilities were measured while the microlensed images were rotating. This strategy allowed us to directly measure $\theta_{\rm E}$ and the microlens-source direction of motion, independently of any reference to the photometric light curve.

On 18 April 2019, Gaia19bld was identified as a transient object by the Science Alerts programme of the Gaia spacecraft (European Space Agency), and intensive

photometric ground-based monitoring was subsequently triggered [9] (Extended Data Fig. 1). On 8 July, our real-time modeling of the light curve indicated that the brightness of Gaia19bld should pass the PIONIER magnitude limit ($H_{\rm lim} = 7.5$ for median atmospheric conditions) at the light curve's peak, which was expected to occur between 12 and 17 July. We thus triggered an observation request on 10 July 2019, as part of our PIONIER Target-of-Opportunity programme. We obtained a first set of interferometric data before the peak, on 12 July, with the four 1.8-m Auxiliary Telescopes at medium baselines configuration (projected baselines of $29 - 90$ m), followed by two additional epochs (19 and 21 July) both collected after the peak with the large baselines configuration (projected baselines of $46-128$ m). On both 12 and 19 July, we obtained two sets of data (*i.e.* two observing sequences) collected about half an hour apart, while we obtained a single observing sequence on 21 July. Details of our observations are provided in the Methods.

As our PIONIER programme initially aimed at imaging, we first used our data to produce reconstructed images for each of the three epochs. In Fig. 1, we present the results obtained with a model-independent algorithm, SQUEEZE [20]. This algorithm makes no assumption on the distribution of light in the plane of the sky, but still unambiguously recovers two typical features of microlensing by an isolated microlens (red-scale patterns): the source is split into two images on either side of the microlens (marked by a white dot), which are furthermore aligned along the white dotted line and rotate as a function of time (the slight asymmetries in the images, in particular for 12 July, are reconstruction artefacts, cf. Methods). From the reconstructed images, we already get a basic information on the value of $\theta_{\rm E}$, as we expect the images (white arc-shaped images from the best-fit model presented below) to be separated by about $2\theta_{\rm E}$ at high magnification, *i.e.* here, $\sim 1 < 2\theta_{\rm E} < 2$ mas. As a matter of fact, Fig.1 displays the very first images of gravitationally-lensed arcs from a distant star, whereas until now, only arcs of galaxies had been reported. Remarkably, Gaia19bld's arcs were captured in rotation around the lens, a unique case amongst all observed gravitationally-lensed images.

We then analysed the PIONIER data assuming an underlying single-lens microlensing model. The (squared) visibilities are shown in the middle panels of Fig. 2, and the closure phases in Extended Data Fig. 2. Each observation comprises six sets of visibilities (one for each of the six baselines) as well as four sets of closures phases (one for each of the four triangles of telescopes), all split into six effective wavelengths. We started by examining the three epochs independently. As detailed in the Methods, the data are not compatible with a point-like model for the source, but are very well fitted by an extended-source model (compare Fig. 2 and Extended Data Fig. 3). The images are then arc-shaped instead of being point-like (see e.g. Extended Data Fig. 4a). Each of the three epochs provides an indepen-

dent measurement of $\theta_{\rm E}$, as well as the direction of the line joining the centre of the two arcs, at the time of the observation (Methods and Extended Data Fig. 5). These directions agree very well with those derived from the non-parametric reconstruction discussed previously (white dotted lines in Fig. 1).

In a second step, we modeled the trajectory of the source relative to the microlens as a straight line, assuming a constant velocity (which is an appropriate assumption here, cf. Methods and Extended Data Fig. 7). The model is detailed in the Methods and the probability distributions of the fitted parameters are shown in Extended Data Fig. 6. The fit of the visibilities is summarised in Fig. 2 (the closure phases will be discussed later): the leftmost panels show the best-fit patterns of the visibility, the middle panels the data and the model, and the rightmost panels the corresponding positions and shapes of the microlensed images (thin arcs, which are also superposed onto the non-parametric reconstruction in Fig. 1). For the plot, we have used the value of ρ (*i.e.* the angular radius of the source in $\theta_{\rm E}$ units) derived from the light curve modelling [9], as it is not constrained by interferometry (that is, the thickness of the arcs, about 0.05 mas, is well beyond the resolution of the interferometer) with no impact on our main results, though (cf. Methods). In particular, we directly measured the angular Einstein ring radius to an unprecedented accuracy, $\theta_{\rm E} = 0.7650 \pm 0.0038$ mas (Fig. 4b), using PIONIER visibilities only.

As Gaia19bld is a relatively long event ($t_{\rm E} \simeq 107$ days), the modeling of the ground-based light curve [9] (cf. Extended Data Fig. 1) provides a fair estimate of the microlens parallax. $\pi_{\rm E}$ is actually the modulus of vector $\vec{\pi}_{\rm E}$, whose direction is the same as the relative microlens-source motion in the geocentric frame, so that in practice, its two north/east (signed) components $(\pi_{{\rm E},N}, \pi_{{\rm E},E})$ have to be measured to yield $\pi_{\rm E}$. These are displayed as blue confidence ellipses in Fig. 3. Although $\pi_{\rm E}$ could not be measured from interferometry alone, as the observations only spawn a short fraction of the event's timescale $t_{\rm E}$, the modelling of the three epochs of PIONIER visibilities provides an independent measurement of the angle of the microlens-source trajectory relative to the East-West direction, $\alpha' = 152.6\ (+180) \pm 0.9^\circ$ (cf. Methods and Extended Data Fig. 4d). These time-series observations also unambiguously settle that the Gaia19bld microlens passed the source star on its lefthand side (Extended Data Fig. 4d), thereby breaking a degeneracy often encountered in microlensing [21]. While the visibilities alone cannot decide between α' and $(\alpha' + 180^\circ)$, the analysis of the closures phases shows that $\alpha' = 152.6 \pm 0.9^\circ$ provides a better fit to the data (Extended Data Fig. 2), which is confirmed by the light curve modelling [9]. Nevertheless, as the two arcs are almost identical, the closure phases do not exceed 5°, which is just above the mean scatter of the data.

From the derivation of α', we now obtain a direct constraint on the ratio

$\pi_{\mathrm{E},N}/\pi_{\mathrm{E},E}$, since it also equals $\tan\alpha' = \tan(\alpha' + \pi)$, which is shown as the grey-shaded area in Fig. 3 for our derived value of $\pi_{\mathrm{E},N}/\pi_{\mathrm{E},E} = 0.517 \pm 0.021$. When this constraint is introduced as a Bayesian prior in the ground-based light curve fit, the parallax becomes very well determined, $\pi_{\mathrm{E}} = 0.0818 \pm 0.0020$ (orange confidence ellipses in Fig. 3). Finally, combining θ_{E} and π_{E} yields the microlens mass, $M = 1.147 \pm 0.029$ $\mathrm{M}_\odot$, measured to an unprecedented accuracy amongst all other microlensing events (Fig. 4). Additionally, low- and high-resolution spectra taken at telescopes of Las Cumbres Observatory Global Telescope Network and with the X-Shooter spectrograph at the VLT allowed to characterise the source star [22], a red giant star of $R_* = 40 \pm 10$ $\mathrm{R}_\odot$, and to determine its distance from Earth, $D_S = 8.4 \pm 1.5$ kpc. The microlens distance follows from $D_L = 1/(D_S^{-1} + \pi_{\mathrm{E}}\theta_{\mathrm{E}}/\mathrm{au})$ (with au the Astronomical Unit), here $D_L = 5.5 \pm 0.6$ kpc.

Beyond demonstrating the potential of optical/infrared interferometry, Gaia19bld also provided an exceptional opportunity to test our analysis against independent measurements, obtained with more classical procedures. In fact, Gaia19bld was also observed with Spitzer around the light curve peak [9], yielding a space-Earth microlens parallax of $\pi_{\mathrm{E}} = 0.0823 \pm 0.0018$, in very good agreement with our result ($\pi_{\mathrm{E}} = 0.0818 \pm 0.0020$, cf. previous paragraph). This benchmark comparison is fortunate, as Spitzer ended its mission in 2020. The combination of spectroscopic data [22] with ground-based, Gaia and Spitzer light curves [9] led to the measurements of θ_{E} using three different methods (hereafter, A, B and C) for the reduction of spectroscopic data: $\theta_{\mathrm{E}}^A = 0.754 \pm 0.013$ mas, $\theta_{\mathrm{E}}^B = 0.724 \pm 0.012$ mas and $\theta_{\mathrm{E}}^C = 0.721 \pm 0.018$ mas, compared to PIONIER measurement alone, $\theta_{\mathrm{E}} = 0.7650 \pm 0.0038$ mas. The three corresponding microlens masses are $M^A = 1.125 \pm 0.031$ $\mathrm{M}_\odot$, $M^B = 1.080 \pm 0.030$ $\mathrm{M}_\odot$ and $M^C = 1.076 \pm 0.036$ $\mathrm{M}_\odot$, in good agreement with our combined analysis of PIONIER and ground-based light curve, $M = 1.147 \pm 0.029$ $\mathrm{M}_\odot$. The similarity of the error bars on the mass for the two approaches means that the uncertainty on π_{E} dominates over the uncertainty on θ_{E}. We can further estimate the angular radius of the source star, $\theta_* = \rho\theta_{\mathrm{E}}$, which reads $\theta_* = 24.50 \pm 0.17$ μas from our PIONIER and ground-based light curve analysis, compared to the three values derived from spectroscopy alone [22]: $\theta_*^A = 24.16 \pm 0.40$ μas, $\theta_*^B = 23.20 \pm 0.38$ μas and $\theta_*^C = 23.11 \pm 0.54$ μas. A last physical parameter we can compare is the microlens-source relative proper motion, $\mu_{\mathrm{rel}} = \theta_{\mathrm{E}}/t_{\mathrm{E}}$, which carries important information on the Galactic kinematics of the event. The combined photometric and spectroscopic analysis [9, 22] yields $\mu_{\mathrm{rel}}^A = 2.57 \pm 0.046$ mas/yr, $\mu_{\mathrm{rel}}^B = 2.47 \pm 0.043$ mas/yr and $\mu_{\mathrm{rel}}^C = 2.46 \pm 0.063$ mas/yr from the three methods respectively, while our combined PIONIER and ground-based light curve value is $\mu_{\mathrm{rel}} = 2.61 \pm 0.018$ mas/yr.

With a mass of ~ 1.1 $\mathrm{M}_\odot$, the microlens could in principle be a solar-type star

or a stellar remnant such as a white dwarf, a neutron star, or even a hypothetical primordial black hole [24]. If the microlens were a main sequence star, its apparent magnitude would be around [22] $H = 18.5 \pm 0.5$ and $V = 20.3 \pm 0.5$. This is unfortunately above the detection limit derived from the light curve analysis, $V < 17$, and well above the PIONIER detection limit of $H_{\rm lim} = 7.5$. Thus our data cannot formally distinguish between a solar-type star and a stellar remnant. However, neutron stars detected to date mostly have masses in the range $1.4 - 1.5$ $M_\odot$, slightly above our mass measurement, and white dwarfs of about 1.1 $M_\odot$ are found to be very rare. Therefore the stellar remnant scenario seems very unlikely. The question may find a definitive answer when the microlens has moved far enough away from the source, in a few years from now. Gaia19bld microlens with then make a perfect target for adaptive-optics observations with future 30m-class telescopes, such as ESO's Extremely Large Telescope.

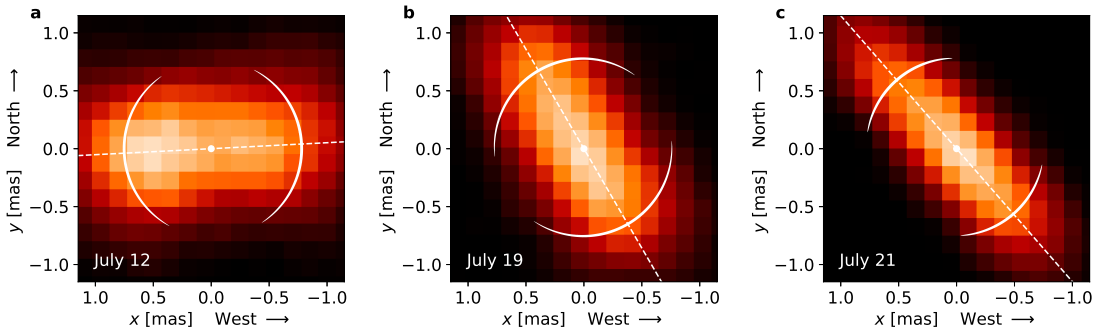

Figure 1: **Gravitationally-lensed arcs in rotation around Gaia19bld's microlens.** From left to right, the red-scale patterns show the model-independent interferometric reconstructions of the microlensed images (in linear scale, from black to white) for each of the three epochs (12, 19 and 21 July 2019) and independently of the others, while the superimposed white arcs are the images of the source derived from the time-dependent best-fit microlensing model. The white dot marks the position of the (unseen) microlens, and the dotted lines join the center of the arcs. The visual unbalance in the non-parametric image reconstructions are trackable artefacts. The figure shows that both the orientation of the arcs and their lengths agree well between the time-dependent model and the individual non-parametric reconstructions. The arcs are not resolved in thickness though, as it is a factor of a hundred below the resolution of the interferometer. The PIONIER time series show that from left to right, the images have rotated by 127° counterclockwise around the lens.

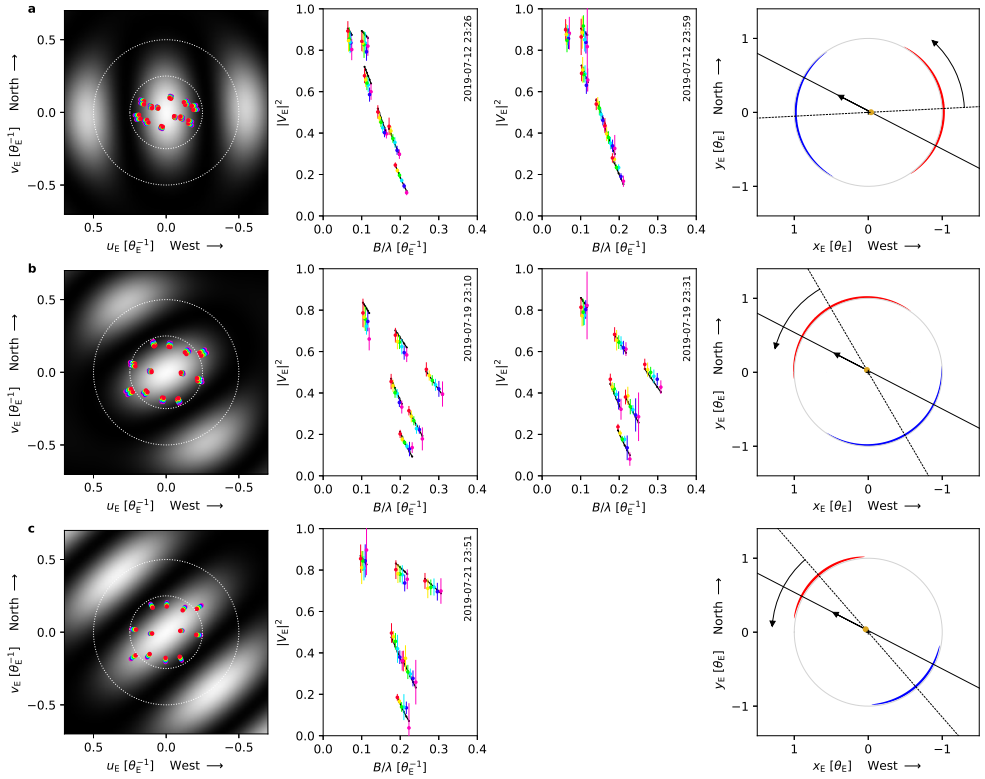

Figure 2: **Gaia19bld's PIONIER squared visibility measurements as a function of time.** Panel **a** corresponds to 12 July (two observing sequences), panel **b** to 19 July (two observing sequences) and panel **c** to 21 July (one observing sequence). Data from 12 July were collected with medium VLTI baselines (longest baseline: 90m), while data from 19 and 21 July were obtained with large baselines (longest baseline: 128m and 126m respectively), which also set the maximum angular resolution of the observations. The leftmost plots (in gray shades) display the collected data in the Einstein $(u_{\rm E}, v_{\rm E})$-plane (in $\theta_{\rm E}^{-1}$ units), *i.e.* six VLTI baselines per observing sequence split into six effective wavelengths, marked by rainbow-colored dots. The best-fit squared-visibility patterns are shown in gray scale ranging from $|V_{\rm E}|^2 = 0$ (black) to 1 (white). The inner dashed circle marks the typical angular resolution, and the outer circle twice the typical resolution. The plots in the middle show the data with their 1-σ error bars (in rainbow colors) as a function of B/λ (in $\theta_{\rm E}^{-1}$ units), where B is the baseline length and λ the observing wavelength. The black lines correspond to the best-fit model (shown only in the vicinity of the data points). The rightmost plots show the geometry of the microlensing event. The microlens (black dot, undetected by the interferometer) is set fixed in the center of the North-East reference frame (both axes are in $\theta_{\rm E}$ units). The blue and red arcs are respectively the major and minor images of the source (which position is marked by a yellow dot), and the dotted line joins the centers of the two arcs. The trajectory of the source relative to the microlens is indicated by the bold straight line with arrow, while the curved arrow indicates the direction of rotation of the arcs.

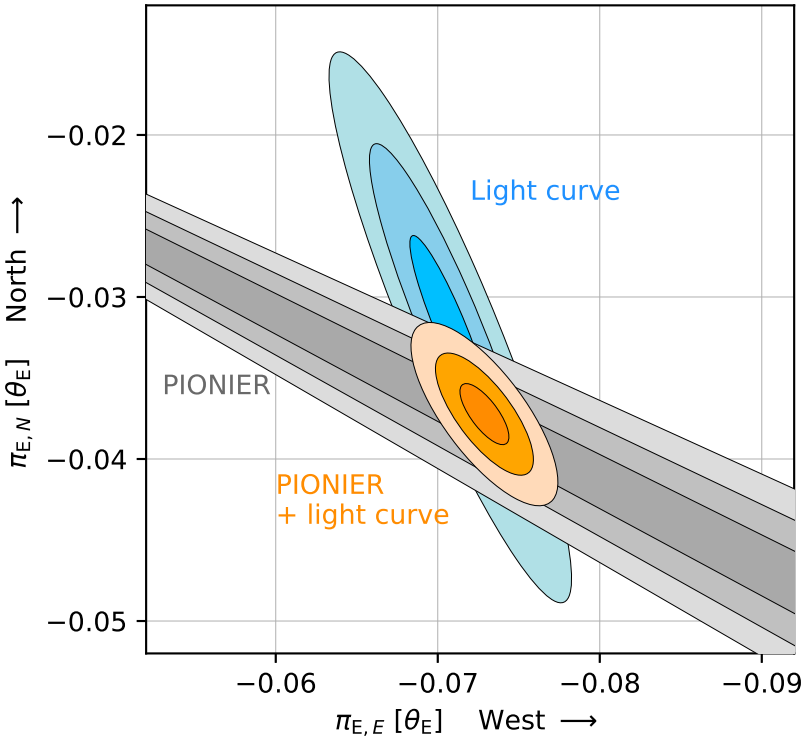

Figure 3: **Microlensing parallax measurement.** The grey-shaded region displays the interferometric constraints on the $(\pi_{\mathrm{E},N}, \pi_{\mathrm{E},E})$ components of the microlensing parallax (1-, 2- and 3-σ confidence levels). The blue ellipses are the constraints obtained from ground-based photometric data alone at the same confidence levels, while the orange ellipses correspond to the combined fit (ground-based photometry and PIONIER interferometry).

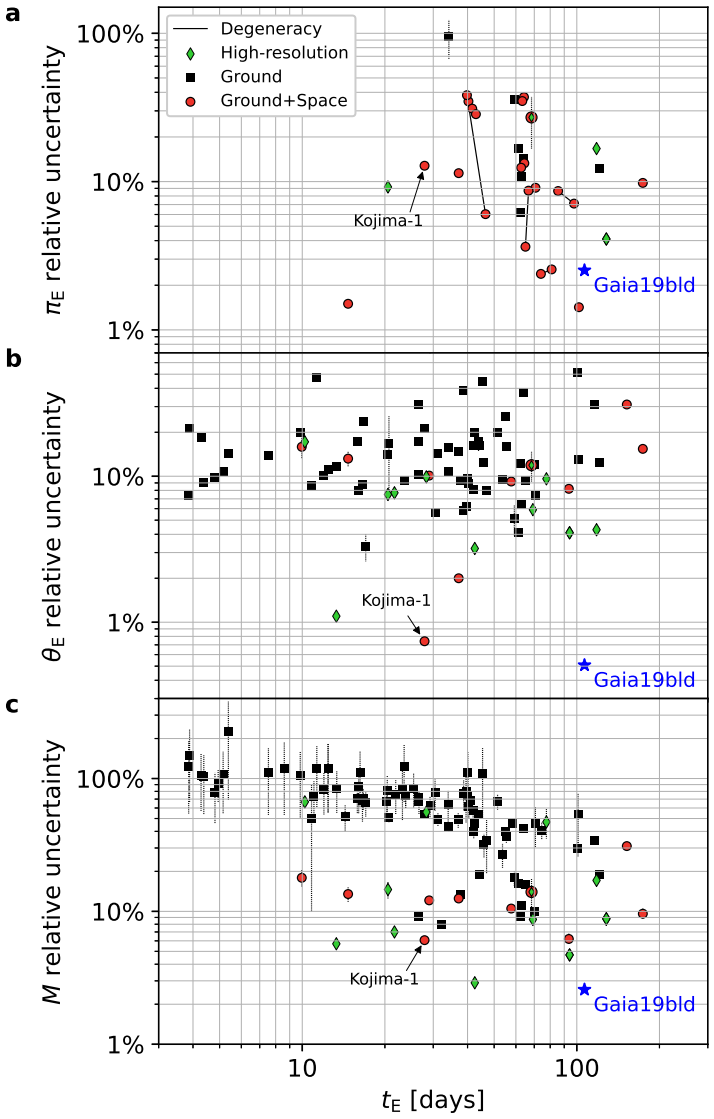

Figure 4: **Accuracy of physical parameter measurements.** The figure shows the relative uncertainties (or $|\sigma_x/x|$, where σ_x is the 1-σ error bar on x) in measurements of microlensing parallax π_E (panel **a**), angular Einstein ring radius θ_E (panel **b**) and microlens mass M (panel **c**), for Gaia19bld (blue star) and for other exoplanetary microlensing events extracted from the NASA Exoplanet Archive and single-lens events from ref. [23], as a function of their Einstein time scale t_E. Ground-based and space-based parallax measurements are respectively shown as black squares and red circles, while green diamonds involve high-resolution imaging. Degenerate measurements of π_E are connected with a black line (data available in Supplementary Tabs. 1, 2 and 3). For 'Kojima-1', the relative uncertainty on θ_E combines interferometry, high-resolution imaging, spectroscopy and space parallax [8, 18, 19], while in the case of Gaia19bld, this uncertainty comes from interferometry alone.

Methods

Basics of interferometric gravitational microlensing. Gravitational microlensing [1] stands today as one of the main methods that allows us to probe the Milky Way populations of brown dwarfs, extrasolar planets [25] and stellar remnants, including isolated stellar mass black holes [26], especially at great distances from the Earth ($\sim$ 1 to 8 kpc). Several thousands of microlensing events have been monitored so far, yielding more than a hundred detections, and made it possible to derive statiscial estimates of the frequency of bound exoplanets in the $\sim$ 0.5 to 10 au range [27, 28] as well as free-floating planets [29, 30].

Microlensing refers to the bending of light rays by an intervening body transiting the line of sight of a distant star (or in an extra-galactic context, a quasar). When the background star (called the 'source') is sufficiently aligned with the foreground object (called the 'microlens'), the light originating from the source is deflected, and a 'microlensing event' occurs. The microlens can be an isolated body, intrinsically luminous or not (like a star or a black hole), or a set of bodies bound by gravity, such as a planetary system. Microlensing affects the shape and the number of images of the source star, which results in a global enhancement of the total flux received by the observer. As the individual images produced by the microlens cannot be separated by classical telescopes, what is usually measured is the increase (hereafter, the 'magnification') of the flux of the source star as a function of time (cf. ground-based light curve of Gaia19bld shown in Extended Data Fig. 1). However, these images can in principle be resolved with long-baseline interferometers, since their typical separation around the magnification peak is of the order of a milliarcsecond, *i.e.* within the reach of an interferometer with baselines of a few tens or a hundred meters.

The typical separations of the images are directly related to the physical value of $\theta_{\rm E}$, the angular radius of the Einstein ring [14] (dashed circle in Extended Data Fig. 4a), which is a function of the microlens mass M, the observer-microlens distance D_L and the observer-source distance D_S through

$$\theta_{\rm E} \equiv \sqrt{\frac{4GM}{c^2}\left(\frac{D_S - D_L}{D_S D_L}\right)}\,, \qquad (1)$$

where c is the speed of light and G the gravitational constant. In a more condensed form, $\theta_{\rm E}$ is usually expressed as $\theta_{\rm E}^2 = \kappa M \pi_{\rm rel}$, where $\pi_{\rm rel} \equiv {\rm au}/D_L - {\rm au}/D_S$ is the relative lens-source parallax (as seen from the Earth) and $\kappa = 8.144$ mas/M$_\odot$, with M expressed in solar masses (M$_\odot$), D_L and D_S in kiloparsec (kpc) and $\theta_{\rm E}$ in milliarcsecond (mas). The Einstein timescale $t_{\rm E}$ is then defined as the time it takes the source to travel one $\theta_{\rm E}$ relative to the microlens. In general, the longer the event's timescale, the higher the mass of the microlens ($t_{\rm E}$ scales as the square root of the lens mass). Very long duration microlensing events are therefore likely

to involve stellar mass black holes. On the other hand, events with very short timescales (less than 2 days) are likely to involve free-floating planets.

When the microlens is formed of an isolated massive body (*i.e.* a 'single microlens', as for Gaia19bld), a perfect point-like source of light would be seen as two point-like images, both located on the same straight line passing through the source and the centre of the microlens. These are shown in Extended Data Fig. 4a as the four black points aligned on the dashed sloping line, with S the source, L the microlens, and I_+ and I_- the two images. The two images are not symmetric, and carry a different flux (more details are given in the modelling section below). This simple 'point-source point-lens' (PSPL) model holds as a good approximation when the angular radius of the source star, θ_*, is much smaller than the Einstein's angular radius, *i.e.* $\theta_* \ll \theta_{\rm E}$, and/or when the angular separation between the microlens and the source β is large compared to $\theta_{\rm E}$, *i.e.* $\beta \gg \theta_{\rm E}$.

Otherwise, the microlens 'resolves' the spatial extension of the images and the model must be replaced by a model with an extended source, what is usually referred to as 'finite-source effects' which affect the shape of the magnification curve (this model is usually called 'extended-source point-lens' model, or ESPL). A typical situation is shown in Extended Data Fig. 4a: the source star (as it would appear in the absence of gravitational microlensing) is the orange disk of radius $\rho = \theta_*/\theta_{\rm E}$ (that is, ρ is the angular source radius expressed in 'Einstein units' $\theta_{\rm E}$) and the two extended images are shown in red and blue, on either side of the Einstein ring. The red image (I_+) is referred to as the 'major' image, because it is the largest and brightest of the two images. The blue one (I_-) is the 'minor' image. Their respective positions relative to the Einstein ring depend directly on the instantaneous separation u_1 between the source and the microlens, expressed in Einstein units (*i.e.*, $u_1 = \beta/\theta_{\rm E}$ from the above). A general property of gravitational lensing is that the surface brightness of the source is preserved; hence the greater the surface of the images, the greater the magnification. A gravitational microlens is furthermore achromatic. As the source approaches the microlens (that means $|u_1|$ decreases), the images lengthen along the Einstein ring and become arc-shaped, and if the microlens is inside the source disk, the two arcs merge into a single ring-shaped image (a case not shown in Extended Data Fig. 4a). The ring is perfect when the alignment is exact, *i.e.* for $u_1 = 0$. As for the microlens, it can always be considered as point-like because it is not gravitationally lensed; for example, a solar-like microlens star at 4 kpc is seen under an angle of about 1 μas, which is several hundreds times below the resolution of any infrared interferometer.

Let us now examine the situation from an interferometric point of view. When finite-source effects are negligible (point-source approximation), the two point-like images are separated by about $2\theta_{\rm E}$ (in the peak magnification region where

Gaia19bld observations are collected) and produce a characteristic sinusoïdal squared visibility pattern, as those shown in the left panels of Extended Data Fig. 3. As finite-source effects become important, and the length of the arcs reaches an appreciable fraction of $2\theta_{\rm E}$, these become resolved by the interferometer and the previous point-source pattern becomes modulated in the direction perpendicular to the line joining the centers of the arcs (cf. left panels of Fig. 2a). When the extension of the arcs is significant, the visibility pattern gradually adopts a circular geometry as the arcs tend towards the formation of a ring. The projected extension of the arcs onto the direction perpendicular to the arcs is $2\theta_{\rm E}\min(|\eta_1|, 1)$, where $\eta_1 \equiv \rho/u_1$. We expect finite-source effects to be detected by interferometry when the images are arc-shaped with significant size (typically, $1 > |\eta_1| > \sim 0.5$), or when they form a ring-shaped image (which happens for $|\eta_1| \geq 1$). Interferometric data then provide a direct measurement of $\theta_{\rm E}$.

As the source moves relative to the microlens (black thick arrow in Extended Data Fig. 4a), the images rotate around the microlens. This is better illustrated in Extended Data Fig. 4b, which shows the source at two consecutive epochs S_1 (orange filled disk) and S_2 (orange circle), with corresponding images labeled (I_{1+}, I_{1-}) and (I_{2+}, I_{2-}) respectively (major arcs are in red, minor arcs in blue). Another trajectory is shown in the same panel, with the source at consecutive positions S_1' and S_2' and corresponding images at (I_{1+}', I_{1-}') and (I_{2+}', I_{2-}'). It illustrates that for small source-microlens separations ($u_1 \ll \theta_{\rm E}$), the arc-like images of a source at S_1 or at S_1' (and also for S_2 and S_2') are almost identical. In any case, multiple epochs interferometric observations allow to trace back the microlens-source trajectory from the orientation of the images in the sky, which yields a direct constraint on the relative source-microlens motion.

PIONIER observations and data reduction. As mentioned in the article, Gaia19bld was alerted as a transient object by the Gaia Science Alerts programme on 18 April 2019, and was subsequently densely followed-up by a network of ground-based telescopes [9]. Gaia19bld's ground-based photometric data and best-fit light curve are shown in Extended Data Fig. 1. All data were taken in the I and V filters, and were aligned to the OGLE I-filter data to display the figure. The best-fit model is shown as the thick black curve (in principle, the I and V light curves slightly differ in the peak region, where limb-darkening differentially affects the curves, but the effect is small and the two curves are almost identical). In order to compare with PIONIER magnitudes, the figure also provides the magnitude scale in the H filter (right vertical axis), obtained after correcting for $E(I-H)$ differential extinction [22]. Since PIONIER (mounted on ATs) limiting magnitude is relatively low ($H_{\rm lim} = 7.5$ under average conditions), it was important to ensure that the microlensing event would be bright enough to be observable. Although

in general it is only possible to predict the date of the peak a few days in advance, Gaia19bld's particularly long time scale ($t_{\rm E} \simeq 107$ days) made it possible to obtain a reliable prediction about a week in advance, and to determine its H magnitude at peak. Gaia19bld was thus confirmed as a firm PIONIER target candidate on 8 July, and intensely monitored and modeled in real time.

We triggered our Target-of-Opportunity (ToO) on 10 July (blue arrow 'Trigger' in Extended Data Fig. 1), waiting for an opportunity at VLTI to perform our observations; since ToO observations do not have priority over observations in visitor mode, we benefited from the kind permission of visiting astronomers to carry out our programme (cf. Acknowledgements). Gaia19bld passed the PIONIER limiting magnitude on 11 July (data above the horizontal dashed red line in Extended Data Fig. 1), and we obtained our first interferometric data sets on 12 July, shortly before the peak of the event. The microlensing event peaked at $H \sim 6.2$ on 16 July. As Gaia19bld was particularly bright, it could also be observed twice after the peak, on 19 and 21 July (blue arrows in Extended Data Fig. 1). On 22 July, the target was already too faint to allow any further PIONIER follow-up, which confirms that $H = 7.5$ is a conservative limiting magnitude for PIONIER for our type of observation (yet still delivering high-quality data).

Although Gaia19bld was a bright microlensing event, it was not an easy target because it was relatively low on the horizon at Cerro Paranal (RA=12:37:32.56, Dec=-66:06:40.90 in J2000), and observable at the beginning of the night only. As for the guiding star, we used the microlensing event itself as it was the brightest star in the field-of-view. Our strategy was originally to obtain several observations spaced by a few hours to a few days, in order to obtain a precise measurement of the angular Einstein ring radius $\theta_{\rm E}$, and possibly to observe the rotation of the images. As we aimed for imaging, PIONIER observations of 12 and 19 July were interleaved with observations of calibration stars, following the pre-defined sequence CAL-SCI-CAL-SCI-CAL, where CAL refers to the calibration star and SCI to the microlensing target. On 21 July, the target was already close to the limiting magnitude and only a CAL-SCI-CAL sequence was obtained. The three calibration stars chosen for this observing program — HD 108356, HD 111496 and HD 111344 — were K-type giants with an H-band magnitude sufficiently low ($H \simeq 6$) to ensure a high enough signal-to-noise ratio, yet close enough to our target's to ensure a consistent instrumental response. Finally, as the target was bright enough, all observations were carried out using the GRISM light beam disperser mode, which provided six spectral channels (and therefore six data) per baseline in the H band, at 1.533, 1.581, 1.629, 1.677, 1.725 and 1.773 μm.

The first epoch (12 July) consisted of two sets of data (or, two observing sequences) collected about half an hour apart ($\rm JD_1 = 2458677.4765$ and $\rm JD_2 = 2458677.4997$) with the medium baselines configuration K0-G2-D0-J3 (projected

baselines of 31, 51, 90, 48, 82 and 68 meters for the first observing sequence, and 67, 48, 49, 29, 87 and 78 meters for the second one). The second epoch (19 July) also consisted of two observing sequences collected about half an hour apart ($JD_1 = 2458684.4656$ and $JD_2 = 2458684.4803$), but using the large baselines configuration A0-G1-J2-J3 (projected baselines of 128, 95, 49, 90, 106 and 84 meters for the first observing sequence, and 127, 85, 48, 90, 103 and 94 meters for the second one). Finally, the last epoch (21 July) consisted of a single observing sequence ($JD_1 = 2458686.4938$) collected with the large baselines configuration A0-G1-J2-J3 (projected baselines of 92, 99, 85, 46, 90 and 126 meters). The interferometric visibilities and closure phases measured on the unresolved calibration stars, extracted from the raw data with the `pndrs` software [10], were used to derive the time-dependent transfer function of the instrument, which was then used to calibrate the visibilities and closure phases of the science target (also extracted with `pndrs`). The reported uncertainties include the statistical uncertainties from each observation, added in quadrature to calibration uncertainties estimated from the different observations of calibration stars. With four telescopes, each observing sequence consists of 36 squared visibilities (six baselines times six effective wavelengths per baseline) and 24 closure phases (four different triangles times six effective wavelengths per triangle).

In order to correctly calibrate the visibility data, we had to further consider an additional systematic error, which is fully correlated with the measured value of the visibility. The experience with PIONIER shows that adding an uncertainty of about 3% on the measured individual visibilities is a conservative choice (i.e., $\sigma' = \sigma + 0.03|V|^2$, where σ' and σ are respectively the new and original error bars), which we adopt here [10]. Another effect we need to consider is that the errors on the visibility are not fully independent between the different spectral channels, as the light comes from a common light beam before being dispersed by the grism. Hence in the fitting procedure, we take into account a partial correlation of 50% affecting the data of the six spectral channels, for each of the four baselines in a given observation (more details are given below). As for the closure phases, the typical expected precision for a $H \sim 6 - 7.5$ target with PIONIER is of order of a few degrees, in line with the observations presented in this work (Extended Data Fig. 2).

Modelling of PIONIER individual epochs. As mentioned in the article, our first step was to analyse independently each of the three PIONIER epochs (12, 19 and 21 July). The fact that we have obtained three epochs well separated in time, allowing the images to rotate and change shape, is first of all a chance to validate the methods presented in this analysis in three different cases (cf. Fig. 1). It is in particular a unique way to investigate the compatibility between $\theta_{\rm E}$ measurements

in various configurations, which is all the more important since in the literature, there is no history of visibility measurements for microlensing events. Arc-shaped images are also an important case as they concern high-magnification events, which are prime targets for interferometry as they are more likely to get bright enough to be observable. Hence the lessons drawn from these observations will be of great help to study observations where only one interferometric epoch is collected (e.g., short duration of the peak above the limiting magnitude, limited availability of the instrument, choice of observing strategy).

The adopted single-lens model (qualitatively described in the first section of the Methods) is shown in Extended Data Fig. 4a. As already stated above, the parameter $u_1 = u_1(t)$ is the distance between the centre of the source and the microlens (expressed in Einstein units $\theta_{\rm E}$) at a given time t, ρ is the source radius (in $\theta_{\rm E}$ units) and α_1 is the angle between the East-West direction and the axis joining the two images. When the source can be considered as point-like (PSPL model), the model parameters are limited to $(\alpha_1, \theta_{\rm E}, u_1)$. In the case of extended arc-shaped images (ESPL model), two more parameters enter the model: the source radius ρ and a linear limb-darkening (LLD) coefficient a_H to describe the source's brightness profile (defined so that the surface intensity on the stellar disc reads $I(r)/I_0 = 1 - a_H \left(1 - \sqrt{1-r^2}\right)$, where r is the fractional source radius, $0 \leq r \leq 1$, and I_0 a normalisation constant). In practice however, ρ and u_1 cannot be measured separately, as this would require the width of the images to be resolved; being of order of $2\rho\theta_{\rm E} \ll \theta_{\rm E}$, such a measurement is usually well beyond the reach of the interferometer. On the other hand, the ratio $\eta_1 = \rho/u_1$ is always well measured, as it is directly linked to the elongation of the arcs (more precisely, $\varphi = 2 \arcsin \min(|\eta_1|, 1)$, where φ is the angle between the two lines limiting the extension of the arcs, cf. Extended Data Fig. 4a). As a result, our finite-source model is described by four parameters: $(\alpha_1, \theta_{\rm E}, \eta_1, a_H)$. The LLD coefficient a_H is not fitted as its impact on interferometric observables (visibilities and closure phases) is very limited; instead, we adopt the value derived from the detailed spectroscopic analysis of the source star [22], $a_H = 0.45$ (which is also the usual approach in light curve modelling). Finally, the interferometric visibilities and closure phases are calculated as two-dimensional integrals over the two arc-shaped images [31].

For each of the three epochs, we fitted the PSPL and ESPL models to the PIONIER visibility data by running several Markov Chain Monte Carlo (MCMC) chains for the corresponding set of parameters, in order to sample their posterior probability distribution, using the `emcee` algorithm [32]. We used standard diagnostics to make sure that the MCMC chains are stationary, that they have converged (beyond burn-in and good mixing between chains) or that they are long enough to avoid the effect of autocorrelation on the results. We have not used in-

formative prior in the process, apart from priors ensuring that the constraint $\rho > 0$ is always satisfied. For all MCMC runs, the error bars on the visibilities σ_i are rescaled as detailed previously. Furthermore, to take into account the correlation between the six spectral channels in a given baseline, we use a log-likelihood of the form $\mathrm{L} = -1/2\ \mathrm{R}^{\mathrm{T}}\mathrm{C}^{-1}\mathrm{R}$, where R is the residuals vector (difference between data points and model), R^{T} is the transpose of R and $\mathrm{C} = c_{ij}$ is the expected covariance matrix of the residuals, with $c_{ii} = \sigma_i^2$ (diagonal terms), $c_{ij} = \rho_c \sigma_i \sigma_j$ for $i \neq j$, and $\rho_c = 0.5$ the correlation coefficient of 50% discussed previously.

As mentioned in the article, the point-source model (PSPL) does not provide any reasonable fit to the data. The posterior probability distributions of the parameters (not shown here) are very poorly defined, and none of the diagnostics listed above are satisfied. To get an idea of the fact that these models are clearly rejected by the data, they are presented in the two central columns of Extended Data Fig. 3: the model parameters are the same as those in Fig. 2 (best-fit ESPL model), except that this time the source is point-like. It is obvious that while the ESPL model describes very well the data (lines and dots in black on the figures), the PSPL model is unambiguously rejected by the data. This clearly demonstrates that the data do indeed probe the length of the arcs, and not just their overall separation.

The detailed posterior distributions of the ESPL fits to the squared visibilities are given in Extended Data Fig. 5, for the three epochs (12 July in the upper panel, 19 July in the middle panel and 21 July in the lower panel). The figure shows that while α_1, θ_{E} and η_1 are almost not correlated for epochs 19 and 21 July, a non-linear correlation between θ_{E} and η_1 is noticeable on July 12. There are two obvious reasons for this. Firstly, on 12 July, the data were taken with the medium baselines configuration, while the two other epochs were taken with the large baselines configuration. Hence, the exploration of the visibility pattern is narrower than for the two other epochs, as can be seen from comparing the leftmost panels of Fig. 2a to Fig. 2b-c. Secondly, by misfortune the baselines on 12 July mainly probed the direction perpendicular to the main visibility pattern, which holds information about the separation of the two arcs, but very little about their individual elongation. In contrast, on 19 and 21 July the longest baselines probed the visibility pattern in the direction corresponding to the elongation of the arcs. We thus expect the parameters to be determined at a lower accuracy on 12 July.

The main results of the modeling of the individual epochs are the following: firstly, the axis joining the two arcs is well determined through the measurement of $\alpha_1 = 3 \pm 2^\circ$ (12 July), $\alpha_1 = 120 \pm 1^\circ$ (19 July) and $\alpha_1 = 131 \pm 1^\circ$ (21 July). This is the first direct evidence of the rotation of lensed images in a microlensing event. As the visibilities are symmetrical by rotating the global image by half

a turn (*i.e.*, inverting the major and minor images), and as the arcs are almost identical, $\alpha_1 + 180^\circ$ also leads to the same global solutions. As we will see later, the analysis of the closure phases indicate that for Gaia19bld, one of the values is preferred over the other one. $\eta_1 = \eta_1(t)$ is also well measured for the different epochs: $\eta_1 = 0.95 \pm 0.06$ (12 July), $\eta_1 = 0.90 \pm 0.01$ (19 July) and $\eta_1 = 0.65 \pm 0.03$ (21 July), but they are of no specific physical interest in this study. The last parameter measured from individual epochs is the angular Einstein ring radius, of main importance here. We obtain $\theta_{\rm E} = 0.798 \pm 0.022$ (12 July), $\theta_{\rm E} = 0.764 \pm 0.005$ (19 July) and $\theta_{\rm E} = 0.765 \pm 0.008$ (21 July). They are all compatible at less than the 1.5-σ level, as shown in Supplementary Fig. 1. These measurements are already of high precision for our purpose, but a fit combining all three epochs allows to reduce the uncertainty on $\theta_{\rm E}$ to an even lower value, as described later.

Non-parametric image reconstruction. For each epoch, in particular just after the observations were made, we tried to reconstruct the images using model-independent interferometric imaging algorithms, in order to obtain a quick information on the images configuration and eventually adjust our observing strategy. Such an example of reconstruction, obtained from the SQUEEZE algorithm [20], is presented in Fig. 1. This reconstruction confirmed that the reconstructed images displayed a clear elongation, in a different direction for each of the three epochs but of similar angular size (about 2 mas in diameter, which is a good order of magnitude for the Einstein ring diameter, 1.5 mas). It is remarkable that the orientation of the reconstructed images (red pattern) agree very well with the axis joining the two arcs (white dotted line) determined through the measurement of α_1 (obtained from the fit of the visibilities). Also, the elongation of the reconstructed arcs agree well with the model prediction (white arcs and width of the red pattern). The arcs are nevertheless too thin to be resolved by the interferometer, as already discussed. Hence, in spite of their limitations, these are the first images of gravitational arcs for a star located within the Milky Way, following the first giant extragalactic arcs imaged in the Abell 370 galaxy cluster [33, 34] in 1986.

Combined modelling of PIONIER time series. As Gaia19bld was both a bright and long-lasting microlensing event, it was possible to collect three epochs spaced by a few days to allow the images to rotate, with two advantages: on the one hand, it improved the accuracy of the $\theta_{\rm E}$ measurement (and check the consistency between individual measurements, as we did in the previous section), and on the other hand, it determined the direction of motion of the source relative to the microlens. We shall now examine these two aspects by first presenting the corresponding microlensing model.

As with individual epochs, the angular Einstein ring radius $\theta_{\rm E}$ is a parameter

of the model, as well as the source size ρ and its limb-darkening coefficient a_H. As for the parameters α_1 and η_1, measured at their date of observation for individual epochs, they must be substituted by parameters describing the trajectory of the source with respect to the microlens (straight black line in Extended Data Fig. 4a), in the North-East reference frame. Given that the time spent in the peak region of the light curve is relatively short compared to the characteristic duration of the microlens event (*i.e.* to the Einstein timescale $t_{\rm E}$, already defined above), we can assume that the trajectory is locally straight and travelled at constant speed (this hypothesis is indeed well verified *a posteriori* as we will see below). Besides $\theta_{\rm E}$ and a_H, we need to consider four more parameters in the model (partly shown in Extended Data Fig. 4a): α', the source-microlens trajectory angle; u'_0, the minimum source-microlens distance in $\theta_{\rm E}$ units; t'_0, the time at u'_0; and $t'_{\rm E}$, which is also the inverse of the source-microlens velocity in Einstein units. We have used a 'prime' ($'$) for these parameters, to distinguish them from parameters with similar meaning but with a trajectory affected by parallax on a longer timespan (see below). However, some of these parameters cannot be measured individually. As stated previously, the thickness of the arcs cannot be measured from interferometry, and only the ratio $\eta'_0 = \rho/u'_0$ can be measured precisely, and not ρ and u'_0 individually. Similarly, $t'_{\rm E}$ cannot be measured directly. This can be understood by examining Extended Data Fig. 4b: a set of source stars of different sizes ρ produce almost similar arcs (three sources are shown in the figure, at two different epochs S_1 and S_2), which cannot be distinguished by the data. Working out the geometry leads to conclude that only the product $t'_* = \rho t'_{\rm E}$ (the source crossing time) can be accurately measured from interferometry.

Hence, our model comprises six parameters, which are $(\alpha', \theta_{\rm E}, \eta'_0, t'_*, t'_0, a_H)$ and where, again, a_H is held fixed. The posterior distribution of these parameters, as well as their values and uncertainties (medians and 1-σ error bars) are shown in Extended Data Fig. 6: $t'_0 = 0.12 \pm 0.07$ (measured from reference date JD $= 2,458,681$, close to the peak of the event), $\eta'_0 = -1.69 \pm 0.05$ and $t'_* = 3.59 \pm 0.07$; we discuss the case of α' in the next paragraph. One of the major results is the highly accurate measurement of the angular Einstein ring radius we derive, $\theta_{\rm E} = 0.7650 \pm 0.0038$ mas. The relative uncertainty on $\theta_{\rm E}$ is about 0.5%, the lowest measured for a microlensing event so far (Fig. 4b). This level of accuracy is in agreement with recent studies that report a fundamental limiting uncertainty of about 0.4% on the measurement of stellar diameters for long-baseline interferometers [35] (and as mentioned previously, it is possible that the PIONIER data gathered on 12 July might have limited somewhat the overall accuracy on $\theta_{\rm E}$).

While with a single interferometric epoch it is not possible to constrain the source-microlens trajectory, in contrast two or more epochs bring important insights on this relative motion. At high magnification, it is important to remember

that the major and minor arcs (respectively in red and blue in Extended Data Fig. 4) are practically indistinguishable in terms of interferometric visibilities. Hence in practice, with two epochs, four trajectories are possible (source moving from S_1 to S_2 in Extended Data Fig. 4c). If a third epoch S_3 is added (assuming that the arcs have turned sufficiently, as is the case for Gaia19bld), only two parallel directions of motion remain possible (Extended Data Fig. 4d). Indeed fitting the visibilities only, we found two possible values for the trajectory angle, $\alpha' = 152.6 \pm 0.9°$ and $\alpha' = -27.4 \pm 0.9°$. In both cases, a single and direct measurement of $\pi_{\mathrm{E},N}/\pi_{\mathrm{E},E} = 0.517 \pm 0.021$ is obtained (cf. main text). The correct value of α' can in principle be recovered from the analysis of the closure phases, as these quantities are very sensitive to any slight asymmetry of the arcs. In fact, as we argued in the main text, the model with $\alpha' \simeq 152.6°$ provides a better fit to the data (black lines in Extended Data Fig. 2) than the other angle (gray lines). This solution is confirmed by the photometric data. Hence not only the ratio $\pi_{\mathrm{E},N}/\pi_{\mathrm{E},E}$ is measured, but also the individual signs of $\pi_{\mathrm{E},N}$ and $\pi_{\mathrm{E},E}$ (here, both are negative values). Extended Data Fig. 4c also illustrates that three interferometric epochs allow to unambiguously determine on which side of the trajectory the source passes the lens, yielding the sign of parameter u'_0.

Gaia19bld microlens mass and distance. The microlens mass can be computed as $M = \theta_{\mathrm{E}}/(\kappa\pi_{\mathrm{E}})$ (cf. main text). $\pi_{\mathrm{E}} \equiv \pi_{\mathrm{rel}}/\theta_{\mathrm{E}}$, the modulus of the microlens parallax $\vec{\pi}_{\mathrm{E}}$, is defined as the lens-source relative parallax $\pi_{\mathrm{rel}} = \mathrm{au}/D_L - \mathrm{au}/D_S$ expressed in units of θ_{E}, with au the astronomical unit, D_L the observer-lens distance and D_S the observer-source distance. Our analysis allowed us to measure θ_{E} and the ratio $\pi_{\mathrm{E},N}/\pi_{\mathrm{E},E}$ (and with less significance, the individual signs of $\pi_{\mathrm{E},N}$ and $\pi_{\mathrm{E},E}$). As we argued in the main text, in the case of Gaia19bld, the ground-based and Gaia light curves together [9] only provide a loose measurement of $(\pi_{\mathrm{E},N}, \pi_{\mathrm{E},E})$, as shown in Fig. 3 (blue ellipses). To improve the parallax measurement, we included a Gaussian prior on the ratio $\pi_{\mathrm{E},N}/\pi_{\mathrm{E},E}$ in the Bayesian analysis (MCMC) of the ground-based light curve, with the mean and standard deviation of $\pi_{\mathrm{E},N}/\pi_{\mathrm{E},E}$ obtained from the fit of the PIONIER data alone. The constraint it places on $(\pi_{\mathrm{E},N}, \pi_{\mathrm{E},E})$ is displayed in gray in Fig. 3. The value and error on π_{E} we get is similar to that obtained by combining ground-based, Gaia and Spitzer data [9], as discussed in the main text. The posterior distributions of the microlensing parameters for the global fit are given in Supplementary Fig. 2 (medians and 1-σ error bars). Here, the parameters t_0, u_0 and t_{E} have the same meaning as t'_0, u'_0 and t'_{E} defined above, except that they correspond to the resulting parallactic source trajectory shown in Extended Data Fig. 7a, instead of the rectilinear motion used in the modelling of the PIONIER data alone. The parallax components $(\pi_{\mathrm{E},N}, \pi_{\mathrm{E},E})$ are measured at a high level of relative accuracy (com-

pare with other measurements in Fig. 4a), and their two-dimensional posterior distribution is displayed in Fig. 3 as the orange ellipses.

As a last check, we verified that the assumption of a straight trajectory to fit the PIONIER time series was justified, by plotting the instantaneous trajectory angle α' as a function of time: in Extended Data Fig. 7b, it can be seen that α' changes by about 1° between 12 and 21 July, which is well within the error bars on α' (grey shaded area). It demonstrates that interferometric data provide robust prior informations about the microlens-source direction of motion, before any parallax is measured. Other important parameters, such as the relative microlens-source velocity $\mu_{\rm rel} = \theta_{\rm E}/t_{\rm E}$, or the angular radius of the source star, $\theta_* = \rho\theta_{\rm E}$, are also derived at high accuracy (main text). It is noteworthy that θ_* can be obtained with no need for a color-magnitude diagram (CMD) and extinction laws, or spectroscopic observations. The results regarding the physical parameters of Gaia19bld are discussed in the main text.

Perspectives. We anticipate that optical/infrared interferometry [36], combined with ground-based photometry, will play a major role in measuring precisely the mass of faint or even non-luminous isolated stellar remnants, which has not been achieved yet for any of the current list of candidates. In fact, interferometric observations will be all the more useful as microlenses have higher masses, because their Einstein ring radii are larger (and so, easier to resolve). Therefore stellar-mass black holes are particularly well-suited targets, especially since they are predicted to exist in vast numbers in the Milky Way [37].

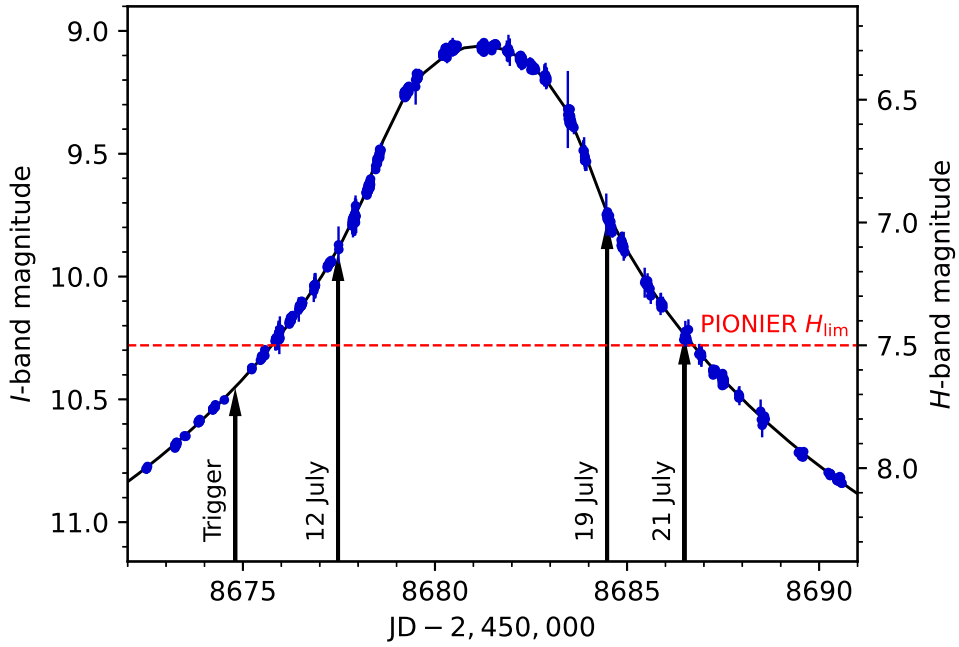

Extended Data Figure 1: **Gaia19bld's light curve near the magnification peak and PIONIER observations.** The black curve is the best-fit light curve to Gaia19bld's photometric data (blue points with 1-σ error bars), shown around the date of maximum brightness. The vertical arrows mark the dates of the Target of Opportunity trigger and of the three PIONIER epochs (12 July, 19 July and 21 July 2019). The photometric data and the light curve are in I-band magnitudes (left vertical axis), while PIONIER data are in H-band magnitudes (right vertical axis), obtained after correcting for differential extinction. The dashed horizontal line is the limiting PIONIER H-band magnitude for median atmospheric conditions.

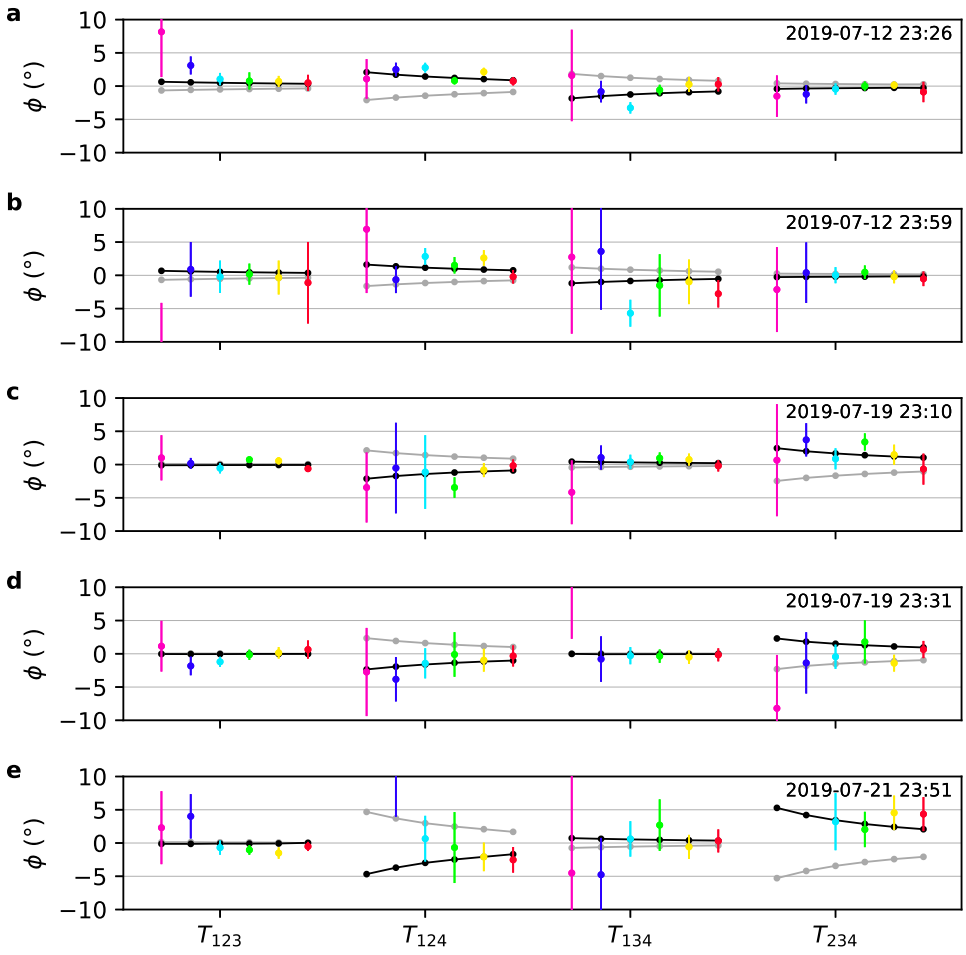

Extended Data Figure 2: **Gaia19bld's PIONIER closure phase measurements as a function of time.** Panels **a** and **b** display the measurements of closure phases (1-σ error bars) for 12 July 2019 (two observing sequences), while panels **c** and **d** correspond to 19 July (two observing sequences) and panel **e** to 21 July (one observing sequence). For each of the four possible triangles of telescopes T_{ijk} (horizontal axis), the rainbow-colored dots with error bars mark the closure phase data split into the six effective wavelengths. The two sets of solid lines with small dots (in black and in gray) show the two possible microlens-source directions of motion (α and $\alpha + \pi$), with the best-fit displayed in black.

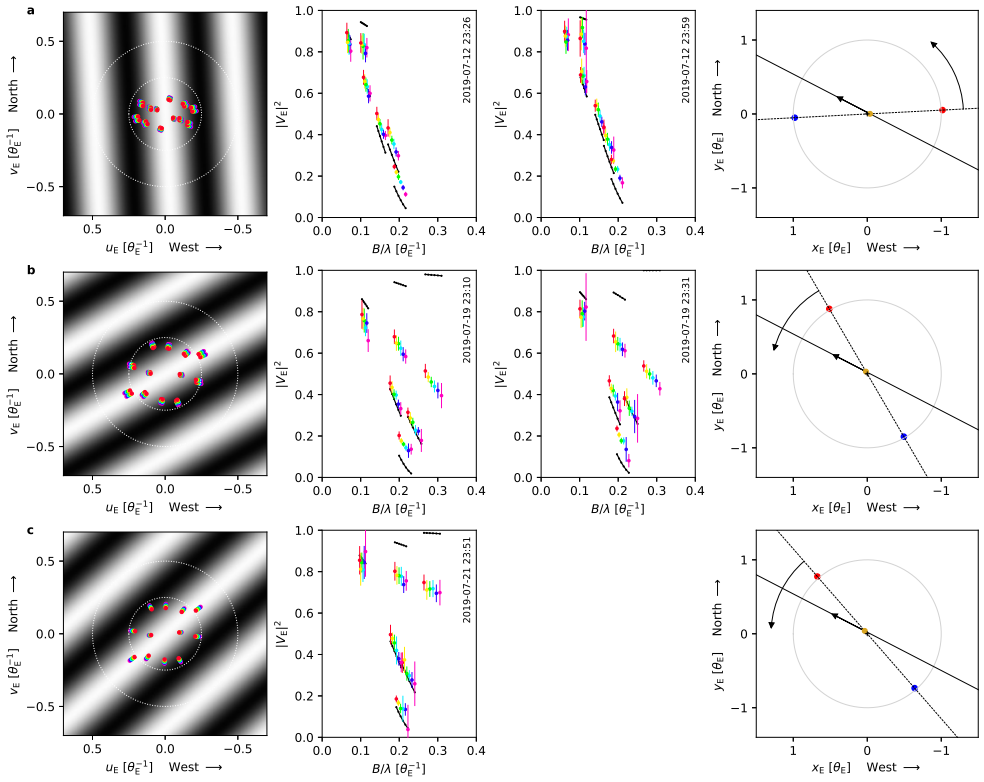

Extended Data Figure 3: **Point-source model of the squared visibilities.** Panel **a** corresponds to 12 July (two observing sequences), panel **b** to 19 July (two observing sequences) and panel **c** to 21 July (one observing sequence). Data from 12 July were collected with medium VLTI baselines (longest baseline: 90m), while data from 19 and 21 July were obtained with large baselines (longest baseline: 128m and 126m respectively), which also set the maximum angular resolution of the observations. The leftmost plots (in gray shades) display the collected data in the Einstein $(u_{\rm E}, v_{\rm E})$-plane (in $\theta_{\rm E}^{-1}$ units), *i.e.* six VLTI baselines per observing sequence split into six effective wavelengths, marked by rainbow-colored dots. The point-source squared-visibility patterns are shown in gray scale ranging from $|V_{\rm E}|^2 = 0$ (black) to 1 (white). The inner dashed circle marks the typical angular resolution, and the outer circle twice the typical resolution. The plots in the middle show the data with their 1-σ error bars (in rainbow colors) as a function of B/λ (in $\theta_{\rm E}^{-1}$ units), where B is the baseline length and λ the observing wavelength. The black lines correspond to the point-source model (shown only in the vicinity of the data points). The rightmost plots show the geometry of the microlensing event. The microlens (black dot, undetected by the interferometer) is set fixed in the center of the North-East reference frame (both axes are in $\theta_{\rm E}$ units). The blue and red dots are respectively the major and minor point-like images of the source (which position is marked by a yellow dot), aligned with the microlens along the dotted line. The trajectory of the source relative to the microlens is indicated by the bold straight line with arrow, while the curved arrow indicates the direction of rotation of the arcs. This figure shows that a point-source model is not a valid approximation here.

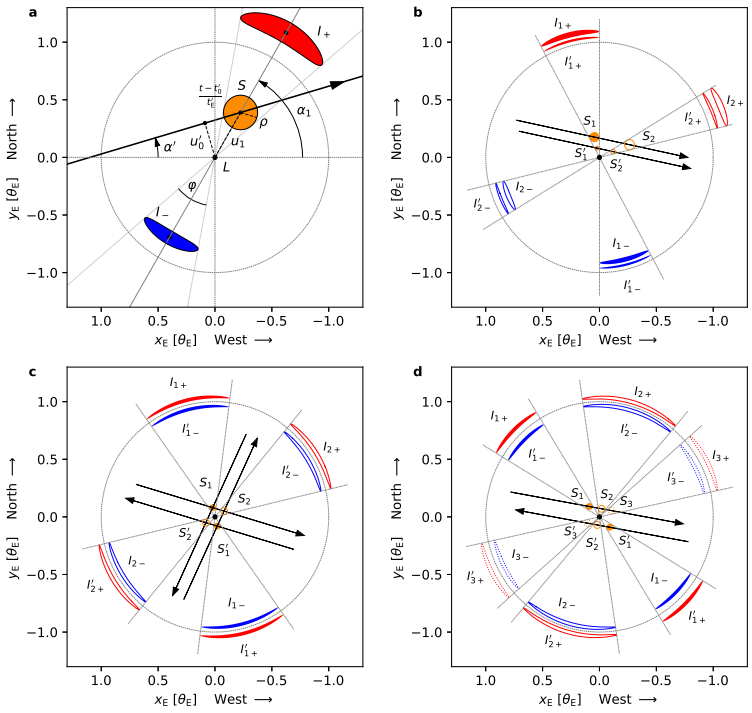

Extended Data Figure 4: **Interferometric microlensing model and constraints on the microlens-source relative motion.** Panel **a** shows the model parameters for a single microlens L (black dot in the center), involving a point-source star (PSPL model) or an extended source (ESPL model). The (unseen) source S is the orange disk, of angular radius ρ in $\theta_{\rm E}$ units (or the black dot in its center for a point source). The trajectory of the source with respect to the microlens is shown as the black thick arrow. It makes an angle α' with the East-West horizontal axis, and u'_0 (in $\theta_{\rm E}$ units) is its signed impact parameter relative to the microlens. The major and minor arc-shaped images of the source are in red and blue respectively (or for a point source, the two black dots in their centers). The line joining the center of the two images makes an angle α_1 with the East-West axis (with the major image up). For single epochs modelling, u_1 is the microlens-source distance in $\theta_{\rm E}$ units. As the source moves relative to the microlens along the black arrow, the images rotate around the microlens. Panel **b** displays the source at two consecutive epochs: S_1 (orange filled disk) and S_2 (orange circle), with corresponding images (major '+' and minor '−') labeled (I_{1+}, I_{1-}) and (I_{2+}, I_{2-}) respectively. Another trajectory is also shown, with the source at consecutive positions S'_1 and S'_2 and corresponding to images at (I'_{1+}, I'_{1-}) and (I'_{2+}, I'_{2-}). The similarity of the arcs for these two scenarii shows that the ratio ρ/u_1 is measured by the interferometric squared visibilities, rather than the two parameters individually. Panels **c** and **d** show that when the major (blue) and minor (red) images are almost identical (which happens at high magnification), four directions of the microlens-source relative motion are possible (panel **c**). When three epochs are obtained, only two possibilities only remain (panel **d**), that can eventually be distinguished by the analysis of closure phases (if the asymmetry between the arcs produces effects above the noise).

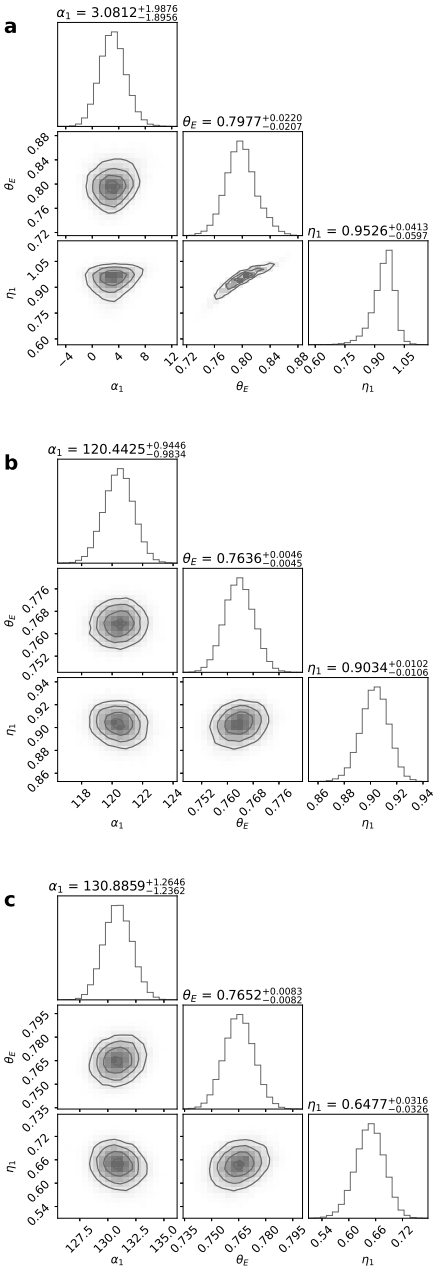

Extended Data Figure 5: **Posterior probability densities of the best-fit parameters when fitting individual PIONIER epochs.** The figure displays the posterior distributions of model parameters α_1 (direction of the line joining the center of the images with respect to the East-West axis), $\theta_{\rm E}$ (angular Einstein ring radius, in mas) and $\eta_1 = \rho/u_1$ (ratio between the angular radius of the source and its distance from the microlens). Panel **a** corresponds to 12 July, panel **b** to 19 July and panel **c** to 21 July. The median values of the best-fit parameters are shown on top of the individual histograms with their 68%-confidence intervals.

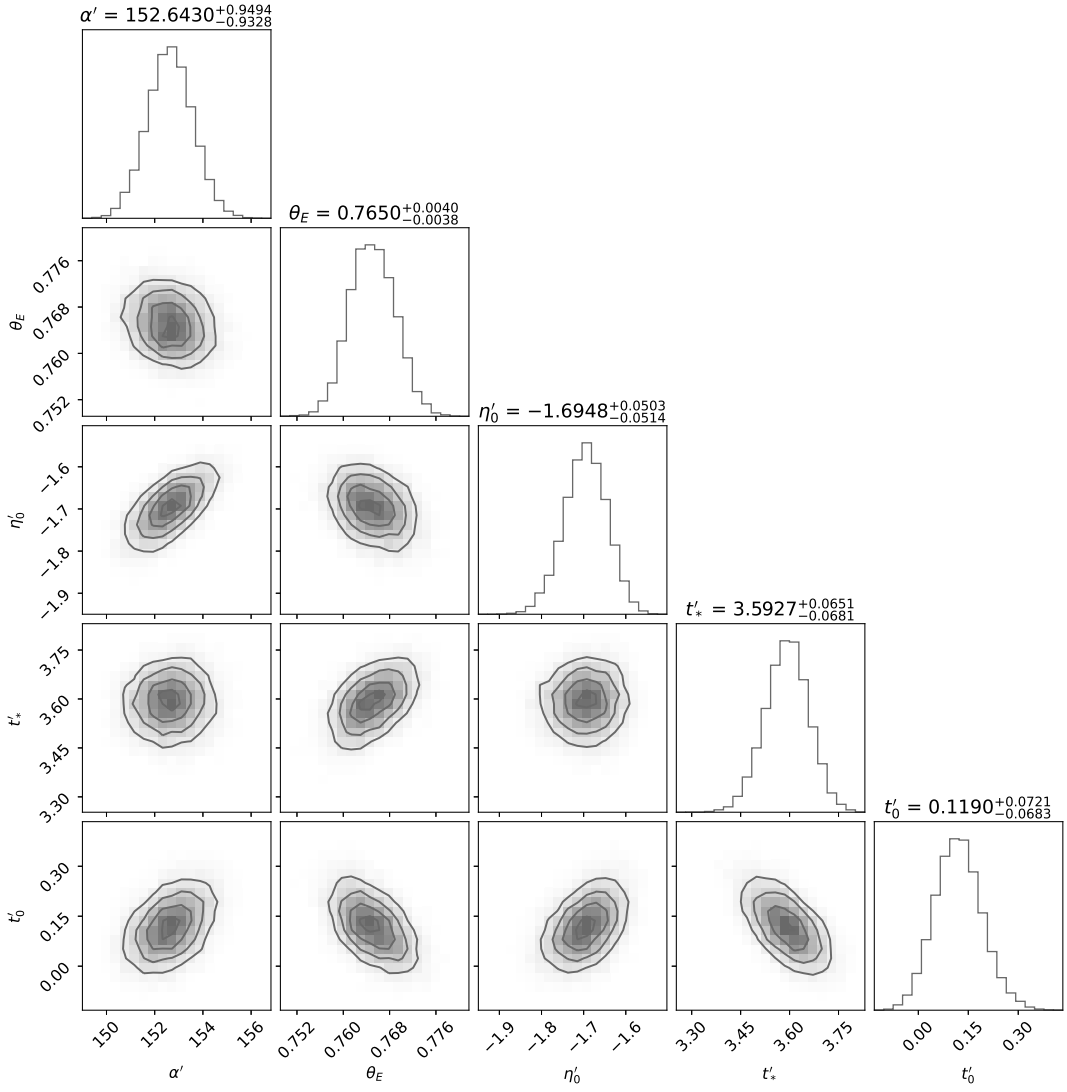

Extended Data Figure 6: **Posterior probability densities of the best-fit model parameters from fitting the three PIONIER epochs.** The figure displays the posterior distributions of model parameters assuming a straight-line trajectory for the source (relative to the microlens). $\theta_{\rm E}$ is the angular Einstein ring radius (in mas), u'_0 is the minimum impact parameter of the source trajectory relative to the microlens (in $\theta_{\rm E}$ units), $\eta'_0 = \rho/u'_0$ is the ratio between the angular radius of the source ρ and u'_0, $t'_* = \rho t'_{\rm E}$ is the product of ρ with $t_{\rm E}$, the time it takes the source to travel an angular distance $\theta_{\rm E}$, and t'_0 is a time reference relative to JD $- 2,458,681$. The median values of the best-fit parameters are shown on top of the individual histograms with their 68%-confidence intervals.

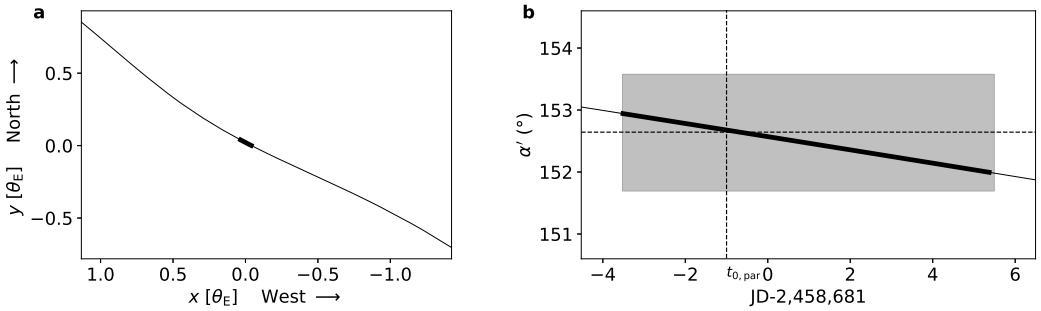

Extended Data Figure 7: **Relative microlens-source trajectory.** Panel **a** shows the source trajectory relative to the microlens in the North-East reference frame obtained by combining the PIONIER data and the ground-based light curve. The thick portion indicates the timespan covered by the PIONIER observations (12 to 21 July). Panel **b** displays the local direction of the same trajectory relative to the East-West axis (quantified by the source trajectory angle α') as a function of time (black line). The gray-shaded region encompasses the values of α' allowed by assuming a straight line trajectory when fitting PIONIER data alone. $t_{0,\mathrm{par}}$ is the reference date for parallax measurement from the light-curve modelling.

References

[1] Paczyński, B. Gravitational microlensing by the Galactic Halo. *Astrophys. J.* **304**, 1-5 (1986).

[2] Gould, A. Measuring the remnant mass function of the Galactic Bulge. *Astrophys. J.* **535**, 928-931 (2000).

[3] An, J. H. First microlens mass measurement: PLANET photometry of EROS BLG-2000-5. *Astrophys. J.* **572**, 521-539 (2002).

[4] Delplancke, F. Resolving gravitational microlensing events with long-baseline optical interferometry. Prospects for the ESO Very Large Telescope Interferometer. *Astron. Astrophys.* **375**, 701-710 (2001).

[5] Dalal, N. & Lane, B. F. Bringing Closure to Microlensing Mass Measurement. *Astrophys. J.* **589**, 199-209 (2003).

[6] Rattenbury, N. & Mao, S. Interferometric visibility and closure phase of microlensing events with finite source size. textitMon. Not. R. Astron. Soc. Lett., **365**, 792 (2006).

[7] Cassan, A. & Ranc, C. Interferometric observation of microlensing events. *Mon. Not. R. Astron. Soc.* **458**, 2074 (2016).

[8] Dong, S. et al. First Resolution of Microlensed Images. *Astrophys. J.* **871**, 70 (2019).

[9] Rybicki, K. et al. Single lens mass measurement in the high magnification microlensing event Gaia19bld located in the Galactic Disk. *Astron. Astrophys.* submitted (2021).

[10] Le Bouquin, J.-B. et al. PIONIER: a 4-telescope visitor instrument at VLTI. *Astron. Astrophys.* **535**, 67 (2011).

[11] Mao, S. et al. Optical Gravitational Lensing Experiment OGLE-1999-BUL-32: the longest ever microlensing event - evidence for a stellar mass black hole? *Mon. Not. R. Astron. Soc. Lett.* **329**, 349-354 (2002).

[12] Bennett, D. P. et al. Gravitational Microlensing Events Due to Stellar-Mass Black Holes. *Astrophys. J.* **579**, 639-659 (2002).

[13] Wyrzykowski, Ł. & Mandel, I. Constraining the masses of microlensing black holes and the mass gap with Gaia DR2. *Astron. Astrophys.* **636**, A20 (2020).

[14] Einstein, A. lens-like action of a star by the deviation of light in the gravitational field. *Science* **84**, 506-507 (1936).

[15] Gaudi, B.S. Microlensing Surveys for Exoplanets. *Annu. Rev. Astron. Astrophys.* **50**, 411-453 (2012).

[16] Calchi Novati, S. et al. Pathway to the Galactic Distribution of Planets: Combined Spitzer and Ground-Based Microlens Parallax Measurements of 21 Single-Lens Events. *Astrophys. J.* **804**, 20 (2015).

[17] Bennett, D. P. et al. Identification of the OGLE-2003-BLG-235/MOA-2003-BLG-53 Planetary Host Star. *Astrophys. J.* **647**, L17 (2006).

[18] Fukui, A. et al. Kojima-1Lb Is a Mildly Cold Neptune around the Brightest Microlensing Host Star. *Astron. J.* **158**, 206 (2019).

[19] Zang, W. et al. Spitzer + VLTI-GRAVITY Measure the Lens Mass of a Nearby Microlensing Event. *Astrophys. J.* **897**, 180 (2020).

[20] Baron, F. et al. A novel image reconstruction software for optical/infrared interferometry. *SPIE* **7734**, 77342I (2010).

[21] Gould, A. et al. Resolution of the MACHO-LMC-5 Puzzle: The Jerk-Parallax Microlens Degeneracy. *Astrophys. J.* **606**, 319 (2004).

[22] Bachelet, E. et al. Spectroscopic follow-up of Gaia19bld. *Astron. Astrophys.* submitted (2021).

[23] Zhu, W. et al. Toward a Galactic Distribution of Planets. I. Methodology and Planet Sensitivities of the 2015 High-cadence Spitzer Microlens Sample. *Astron. J.* **154**, 210 (2017).

[24] Clesse, S. & García-Bellido, J. Seven hints for primordial black hole dark matter. *Phys. Dark Universe* **22**, 137-146 (2018).

[25] Mao, S. & Paczynski, B. Gravitational microlensing by double stars and planetary systems.*Astrophys. J.* **374**, L37-L40 (1991).

[26] Wyrzykowski, Ł. et al.Black hole, neutron star and white dwarf candidates from microlensing with OGLE-III. *Mon. Not. R. Astron. Soc. Lett.* **458**, 3012-3026 (2016).

[27] Cassan, A. et al. One or more bound planets per Milky Way star from microlensing observations. *Nature* **481**, 167 (2012).

[28] Suzuki, D. Microlensing Results Challenge the Core Accretion Runaway Growth Scenario for Gas Giants. *Astrophys. J.* **869**, 34 (2018).

[29] Sumi2011, T. Unbound or distant planetary mass population detected by gravitational microlensing. *Nature* **473**, 349-352 (2011).

[30] Mróz, P. et al. No large population of unbound or wide-orbit Jupiter-mass planets. *Nature* **548**, 183 (2017).

[31] Cassan, A. Interferometric visibility of single-lens models: the thin-arcs approximation. arXiv:2109.11947 (2021).

[32] Foreman-Mackey, D. et al. emcee: The MCMC Hammer. *PASP* **125**, 306-312 (2013).

[33] Lynds, R. & Petrosian, V. Giant luminous arcs in galaxy clusters. *Bull. Am. Astron. Soc.* **18**, 1014 (1986).

[34] Soucail, G. et al. A blue ring-like structure in the centre of the A 370 cluster of galaxies. *Astron. Astrophys.* **72**, L14-L16 (1987).

[35] Gallenne, A. et al. Fundamental properties of red-clump stars from long-baseline H-band interferometry. *Astron. Astrophys.* **616**, 68 (2018).

[36] Schaefer, H. G. et al. Interferometry in the Era of Time-Domain Astronomy. *Exp. Astron.* **46**, 421 (2018).

[37] Wiktorowicz G. et al. Populations of Stellar-mass Black Holes from Binary Systems. *Astrophys. J.* **885**, 1 (2019).

Data Availability

The VLTI/PIONIER data (programme 0103.C-0522(A)) are available at ESO Science Archive Facility (http://archive.eso.org/scienceportal/home).

Acknowledgements

Our PIONIER observations were made under the European Southern Observatory (ESO) programme 0103.C-0522(A). We would like to thank the teams who interrupted or postponed their visitor-mode observing runs to accommodate our time-critical observations, in particular Karine Perraut (12 July, GTO GRAVITY, P.I. Garcia Lopez) and Stefan Kraus (19 and 21 July), as well as the observers (Konrad

Tristam, Aaron Labdon) and the astronomers who assisted us to make these observations a success (Claudia Paladini, Christian Hummel, Linda Schmidtobreick, Fernando J. Selman and the ESO Paranal team at large). We also thank Antoine Mérand for his management of possible conflicts between ToO programmes. A.C. acknowledges the support of Sorbonne Université grants Émergence@Sorbonne-Universités 2016 and Émergence-UPMC 2012. O.A. acknowledges funding from F.R.S.-FNRS. Ł.W. acknowledges support from the Polish NCN grants: Harmonia No. 2018/30/M/ST9/00311 and Daina No. 2017/27/L/ST9/03221. K.A.R. acknowledges support from the Polish NCN grant Preludium No. 2017/25/N/ST9/01253. Y.T. acknowledges the support of DFG priority program SPP 1992 'Exploring the Diversity of Extrasolar Planets' (TS 356/3-1). We would like to thank the reviewers whose comments helped to improve the manuscript.

Author Contributions Statement

A.C. led the analysis, contributed to the observations, performed the modeling of the PIONIER data, wrote the paper. C.R. contributed to the observations, contributed to the modeling of PIONIER data. O.A. contributed to the observations, performed the reduction of the raw PIONIER data. Ł.W. alerted Gaia19bld as a target for our programme, contributed to the observations. K.A.R. contributed to the observations, performed the modeling of the photometric data (published separately). É.B. performed the analysis of the spectroscopic data (published separately). J.-B.L.B. performed the non-parametric reconstruction of the microlensed images. M.H., R.S., J.S., Y.T., J.W. and O.W. participated in the scientific discussion. All authors discussed the results and commented on the manuscript.

Competing Interests Statement

The authors declare no competing interests.